Hydroxyapatites as Versatile Inorganic Hosts of Unusual Pentavalent Manganese Cations

Aurea Varela, Isabel Gómez-Recio, Laura Serrador, María Hernando, Emilio Matesanz, Almudena Torres-Pardo, María Teresa Fernández-Díaz, Jose L Martínez, Francisco Gonell, Gwenaelle Rousse, et al.

Hydroxyapatites as Versatile Inorganic Hosts of Unusual Pentavalent Manganese Cations

Aurea Varela, Isabel Gómez-Recio, Laura Serrador, María Hernando, Emilio Matesanz, Almudena Torres-Pardo, María Teresa Fernández-Díaz, Jose L. Martínez, Francisco Gonell, Gwenaelle Rousse, Clément Sanchez, Christel Laberty-Robert, David Portehault,* José M. González-Calbet, and Marina Parras*

Contrary to molecular species, only very few solids are reported to host manganese (V) species. Herein, we report three new compounds with a hydroxyapatite structural backbone built on the $Mn^{V}O_4^{3-}$ anion: $Sr_5[(Mn_{1-x}Si_x)O_4]_3(OH)_{1-3x}$ (x = 0 and 0.053), $Sr_5(MnO_4)_3(OH)_{1-y}F_y$ (y = 0.90), and $Sr_5[(Mn_{1-x}Si_x)\text{-}O_4]_3F_{1-3x}$ (x = 0.058). These solids are fully characterized using powder X-ray and neutron powder diffraction, scanning trans-mission electron microscopy, electron energy loss spectroscopy (EELS), thermogravimetric analysis, and magnetic measurements. Especially, we report for the first time EELS Mn−$L_{2,3}$ spectra of manganese with the oxidation state (V). Contrary to other Mn(V) oxides, these solids and the nominal compound $Sr_5(MnO_4)_3OH$ do not comprise Ba^{2+} cations but rely only on Sr^{2+} cations, showing that barium is not a required element to stabilize Mn(V) species in inorganic solids. We show that by tuning soft chemistry conditions on the one hand and post-treatment topological transformation conditions on the other hand, Mn(V) and hydroxyl groups can be substituted by Si(IV) and fluoride ions, respectively. Hence, we deliver solids with a potentially wide composition range. These compounds show significant oxygen anionic conduction, thus suggesting the emergence of new functional materials built from high-oxidation state manganese cations.

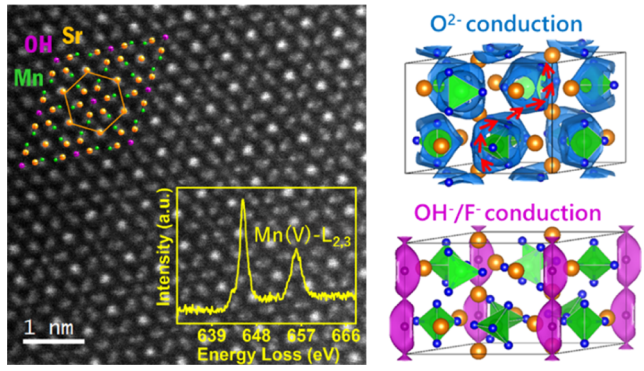

INTRODUCTION

The ability of manganese to adopt various oxidation states determines many combinations of chemical doping and anionic vacancies. These features give rise to a rich variety of oxides, structural dimensionalities, and physicochemical properties, especially electrical, optical, magnetic, and catalytic ones. In most of these oxides, manganese is present as Mn(III) and/or Mn(IV). Mn(V) complexes are numerous,[1−4] thanks to organic moieties that provide a versatile platform for stabilizing Mn(V) species. Noteworthy, some examples of Mn(V) complexes are inspired by the oxygen-evolving complex in the photosystem II for the production of dioxygen during photosynthesis.[3,4] Structural flexibility is more arduous to achieve in nonmolecular inorganic solids, which explains the rare occurrence of Mn(V), especially in oxides. In oxides, Mn(V) is always encountered in a tetrahedral coordination as the $Mn^{V}O_4^{3-}$ anion.

One of the few oxides containing only Mn in the oxidation state V is $Ba_3Mn_2O_8$, which has been revealed as a layered spin dimer compound.[5,6] Besides the interesting magnetic behavior of Mn(V)-containing solids, they show strong optical absorption because of the $Mn^{V}O_4^{3-}$ building unit that produces green-colored compounds of great potential as inorganic pigments such as $Ba_5(MnO_4)_3Cl$ and $Ba_5(MnO_4)_{3-x}(M'O_4)_xCl$ (M′: Cr or P) crystallizing in the apatite structure.[7,8] The $Mn^{V}O_4^{3-}$ anion has been described concomitantly with the presence of Ba^{2+},[9,10] Sr^{2+},[9,10] and/or alkali Li^+, Na^+, and K^+[9−11] in the cationic sublattice. Ba^{2+} is encountered most often in Mn(V) compounds and stabilizes Mn(V) in tetrahedral coordination because of its high basicity that increases the Mn−O bond covalent character.[12] Sr^{2+} should play a similar role, but this has been only scarcely addressed. Indeed, a Sr/Mn oxyhydroxide $Sr_2(Mn^{V}O_4)OH$ has been described fifty years ago without any further mention to it until now.[13] The existence and precise composition of this compound may have strong implications for further design of

high-oxidation state Mn compounds and therefore call for in-depth scrutiny. Indeed, in their original report, Baran et al.[13] indexed the whole powder X-ray pattern on the hydroxyapatite $Ca_5(PO_4)_3OH$-type structure.[14,15] Nonetheless, this structural type is not consistent with the stoichiometry $Sr_2(MnO_4)OH$ proposed for the compound[13] so that both structure and composition of this peculiar solid must be questioned.

The apatite-type structure of general formula $A_5(MO_4)_3X$ (A = Ca^{2+}, Sr^{2+}, Ba^{2+}, or Pb^{2+}; M = P^V, Mn^V, Cr^V, or V^V) and (X = OH^-, F^-, or Cl^-)[8,16,17] consists in (Figure 1) isolated MO_4^{3-}

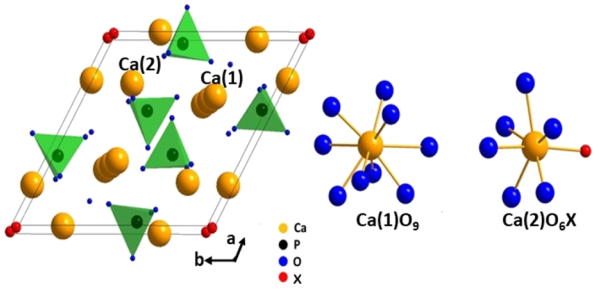

Figure 1. Apatite $Ca_5(PO_4)_3X$-type structure (X: OH^-, F^-, or Cl^-). On the right are shown the two coordinations for Ca: nine-coordinated CaO_9 tricapped trigonal prisms and a seven-coordinated one forming AO_6X bicapped trigonal prisms.

tetrahedra with A cations located in two different environments: a seven-coordinated one forming AO_6X bicapped trigonal prisms and a nine-coordinated one in AO_9 tricapped trigonal prisms. The X anions (OH^-, F^-, or Cl^-) occupy channels running along the *c* axis. These channels favor ionic mobility, which is at the origin of the conducting and catalytic properties of apatites.[18−23]

In this paper, we fully address the composition and structure of the previously reported Sr/Mn(V) hydroxyapatite by revisiting its composition into $Sr_5[(Mn_{1-x}{}^VSi_x)O_4]_3(OH)_{1-3x}$ and by scrutinizing the anionic sublattice through neutron diffraction. We then describe a silicon-free $Sr_5(Mn^VO_4)_3OH$ solid, and we also extend the synthesis and characterization to its corresponding fluoride-substituted apatites where fluoride ions occupy the channels. These results show the versatility of the apatite framework to accommodate a large variety of Mn(V)-based compositions. Finally, we assess their functional response, moving from the well-documented coloring properties because of the $Mn^VO_4^{3-}$ unit to the impact of the various substitutions on the less-explored magnetic and ionic conduction properties, hence paving the way to a new family of manganese-based functional materials.

EXPERIMENTAL SECTION

The preparation of Sr/Mn hydroxyapatites is based on a modification of the synthesis pathway described by Baran et al.[13] In a borosilicate glass round flask, 75 mL of a 10 M NaOH (Aldrich, 97%) solution is added dropwise over 30 mL of a 1.26 M $KMnO_4$ (Aldrich, 99%) solution, under an Ar atmosphere, reflux conditions, and vigorous stirring. After 10 min, 25 mL of a 1.65 M $SrCl_2{\cdot}6H_2O$ (Aldrich, 99%) solution is added dropwise. The whole reaction medium is then kept under reflux conditions for 90 min. After hot filtration, the recovered precipitate is washed with 20 mL of a 2.5 M NaOH solution, 30 mL of a 0.5 M NaOH solution, and 50 mL of hot water. Finally, the powder is dried overnight at 80 °C. To avoid silicon doping, a Si-free hydroxyapatite has been prepared by the same experimental procedure just replacing the glass flask by a Teflon round-bottom flask.

The fluorination of the samples was achieved by grinding different amounts of each of the abovementioned hydroxyapatite phases with polytetrafluoroethylene.[24] The mixture was put in an alumina crucible not covered, and the reaction was performed in air to burn off any residual carbon from the polymer. The optimum reaction conditions correspond to a Mn/CF_2 molar ratio of 1:0.25 and to a temperature of 325 and 350 °C for samples with and without silicon, respectively, applied for 12 h. The products retain their original green color. Higher polymer content and lower reaction temperatures did not result in any noticeable reaction, whereas higher temperatures resulted in SrF_2 impurities that indicate collapse of the hydroxyapatite structure.

X-ray diffraction (XRD) patterns were recorded in a PANalytical X'pert-PRO diffractometer equipped with an X-ray source working with Cu Kα_1 radiation at 45 kV and 40 mA, with a primary beam monochromator and X'Celerator fast detector, in the 2θ range 5−120°, using a step size of 0.017° and an integration time of 200 s at each step. The *in situ* high-temperature XRD (HT-XRD) study was carried out in a PANalytical X'Pert-PRO with an Anton Paar HTK2000 high-temperature chamber working in still air from 20 to 1100 °C. Powder XRD patterns were then recorded with Cu Kα in the 10−80° 2θ range, using a step size of 0.033° and a collection time of 100 s with an X'Celerator fast detector at each step. XRD patterns were recorded each 100 and 50 °C under heating and cooling conditions, respectively.

Neutron powder diffraction (NPD) measurement was performed at the Institut Laue Langevin, Grenoble (France), on the D2B diffractometer (λ = 1.594 Å).[25] The data were analyzed with the Rietveld method[26] using the software package FullProf.[27] Further details on the crystal structure of these apatites were deposited to the joint CCDC/Fiz Karlsruhe database via https://www.ccdc.cam.ac.uk with the following reference numbers CSD-2038883 (HApMn), CSD-2038884 (HApMnSi), CSD-2038881 (FApMn), and CSD-2038882 (FApMnSi).

Thermogravimetric analysis (TGA) was performed using a TG/DTA 6300 SII EXSTAR. About 15 mg of the sample was heated inside a Pt crucible, at a constant rate of 6 °C min^{-1} up to 1100 °C, under an air atmosphere.

Samples for transmission electron microscopy (TEM) were ultrasonically dispersed in n-butanol and transferred to coated copper grids. Selected area electron diffraction experiments and high-resolution TEM were performed on a JEOL JEM300FEG electron microscope. Crystal-by-crystal chemical microanalysis was performed by energy-dispersive X-ray spectroscopy (EDS) carried out on a JEOL JEM 2100 electron microscope supplied with an Oxford INCA detector. The average cationic composition of the samples was determined on a JEOL JXA-8900 "Super Probe" Electron Probe microanalyzer with five wavelength-dispersive X-ray spectrometers operating at 20 kV and 50 μA. The atomic resolution study was carried out on a JEOL JEMARM200cF aberration-corrected STEM electron microscope (Cold Emission Gun) operating at 120 kV (probe size ~0.08 nm). Inner and outer collection semiangles of 68 and 280 mrad, respectively, were employed for high-angle annular dark-field (HAADF) imaging with a nominal camera length of 60 mm. Images of medium size (512 × 512 pixels) were recorded over a total acquisition time of 38 s per frame using a probe current of 10 pA to minimize electron-beam damage. Electron energy loss spectroscopy (EELS) experiments were acquired using a GIF-QuantumER with a collection semiangle of 18 mrad and a convergence semiangle of 20.3 mrad. The Mn oxidation state was analyzed from the energy-loss near-edge fine structure (ELNES) of Mn−$L_{2,3}$ signals. ELNES spectra were acquired over ~0.5 nm area with energy dispersion of 0.05 eV and 2 mm spectrometer aperture. The total acquisition time was optimized in order to prevent beam damage of the sample (see the Supporting Information). The dual-EELS function of the GIF-QuantumER spectrometer, allowing the simultaneous acquisition of two different energy ranges, was used to record simultaneously zero-loss peak (0.0001 s exposition time, 10 frames) and Mn−$L_{2,3}$ core region in order to minimize the uncertainty on the energy shift of the Mn−$L_{2,3}$

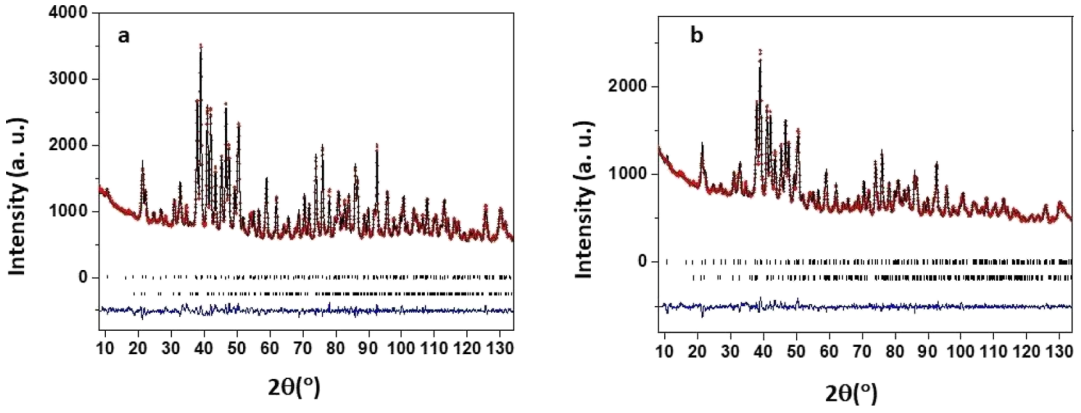

Figure 2. Final Rietveld refinement of the NPD data for (a) HApMn and (b) HApMnSi. The observed patterns (red circles), calculated patterns (continuous black line), and difference curves (continuous blue line) are shown. Upper tick marks correspond to the main apatite phase and lower ticks correspond to $SrCO_3$ added as a secondary phase.

edges. Low-temperature EELS was performed using a double tilt (±24°) liquid nitrogen-cooled specimen holder Gatan 636.

Magnetic measurements were performed on a vibrating sample magnetometer, with a temperature range from 2 to 400 K and an external magnetic field up to 9 T, in a Physical Property Measurement System platform (PPMS-9T).

The conductivity was measured through the thickness of the pellets made by pressing the powders. The ceramic pellets were studied using a homemade two-electrode setup, using an AC impedance/gain-phase analyzer (Solartron SI 1260, UK) with ionically blocking gold electrodes (deposited by gold sputtering) within a high-temperature furnace under air from 200 to 500 °C. The dimensions of the ceramic (13 mm in diameter and ∼1 mm thick) were used to estimate the conductivity. The impedance plots were measured with an increase of 50 °C. Impedance data were recorded after stabilization of 2 h at the dwell temperature. The applied frequency was varied from 1 to 10^6 Hz with an amplitude of 100 mV at 0 V. The resistance of the pellet at various temperatures was estimated from the intercept of the Nyquist plot with the real axis. Bond valence energy landscape (BVEL) maps were generated according to the method developed by Adams,[28] using the program BondSTR as implemented in the FullProf Suite.[27,29] For the BVEL maps, calculations of anionic conduction paths were performed considering cationic neighbors up to 10 Å.

RESULTS AND DISCUSSION

Strontium/Manganese Hydroxyapatite Synthesis and Composition. The Sr/Mn (Sr/Mn = 5:3 mol.) oxyhydroxide (named hereafter HApMn) was prepared by reacting $KMnO_4$ and $SrCl_2$ in a high-concentration aqueous KOH solution (details in the Experimental Section) within a Teflon vial. According to scanning electron microscopy, the resulting dark green powder is constituted by facetted hexagonal particles (Figure S1). The XRD pattern (Figure S2a) is fully indexed on a hexagonal lattice with refined unit cell parameters a = 9.9559(1) and c = 7.45452(7) Å. We observe a remarkable similarity between the recorded pattern and the one of the $Ca_5(PO_4)_3OH$ hydroxyapatite.[14,15] EDS analysis gives a Sr/Mn elemental ratio of 5:3, close to the expected composition. Both results fully agree with a compound adopting the structure type of $Ca_5(PO_4)_3OH$ hydroxyapatite. Performing the same reaction but in a borosilicate vial yields again a dark green solid with a very similar XRD pattern (Figure S2b), indexed on the hexagonal lattice of hydroxyapatite with refined unit cell parameters a = 9.9583(1) and c = 7.4465(1) Å. However, EDS yields a Sr/Mn ratio of about 2:1, which is in stark contrast with the expected composition from the hydroxyapatite structural model described above and with the compound obtained in a Teflon vial. A more precise assessment of the composition was performed using an electron microprobe, which detects a small amount of Si, giving a molar cationic ratio Sr/Mn/Si = 5:2.82:0.18 which strongly suggests incorporation of Si as a dopant substituting Mn, with an overall composition Sr/(Mn,Si) of 5:3, as expected for the hydroxyapatite framework. Silicon originates from the dissolution of the glass vial walls in the highly basic aqueous solution. Therefore, the correct formula of the compound obtained in a glass vial in the present report and also presumably in the original work of Baran et al.[13] is $Sr_5[(Mn_{0.94}Si_{0.06})O_4]_3(OH)_{0.82}$ (referred in the following as HApMnSi), where the OH content is adjusted by charge balance if one considers that all manganese is present as Mn(V). This assumption is further corroborated by EELS (see below) and the OH content is also confirmed by neutron diffraction (see below).

Strontium/Manganese Hydroxyapatite Structure. We assessed the precise structure of the new $Sr_5(MnO_4)_3(OH)$ (HApMn) hydroxyapatite and of its substituted $Sr_5[(Mn_{0.94}Si_{0.06})O_4]_3(OH)_{0.82}$ (HApMnSi) compound using hydrogen-sensitive NPD. The NPD patterns (Figure 2) were refined (Tables S1 and S2) using the hexagonal $Ca_5(PO_4)_3OH$ hydroxyapatite with a space group $P6_3/m$ (ICSD203027) as a starting structural model.[30,31] The large background observed in the NPD patterns is associated to the incoherent scattering of hydrogen from hydroxyl ions and water molecules adsorbed, as shown by thermogravimetric and XRD thermal analyses (see below and Figures S11−S14). Note that a small amount (less than 4% mass) of $SrCO_3$ is detected by NPD (Figure 2). This minority secondary phase is probably related to aging of the sample despite our efforts to prevent exposition of the samples to air from the synthesis to the XRD and then NPD experiments. The H atoms of the OH groups can be evidenced by the scattering density Fourier difference maps (Figure S3) obtained by refinement of the NPD data without including H atoms in the starting $Ca_5(PO_4)_3OH$ structural model. Indeed, the scattering density section x = 0 (Figure S3) shows a weak negative scattering located at $z \sim 0$ and ∼0.5 next to O_H positions, which corresponds to H atoms bonded to oxygen: hydroxyl groups. The final refinement includes the hydroxyl hydrogen refined positions (Table S1).

Strontium in the Sr(1) site (Figure 3) is coordinated to nine oxygen atoms in a tricapped trigonal prismatic arrangement

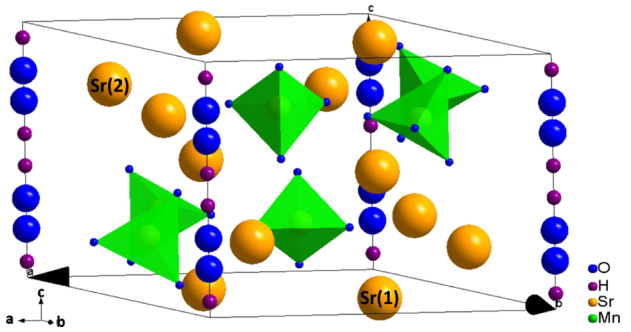

Figure 3. Crystal structure representation for HApMn. The configuration of hydroxyl groups is statistically disordered in such a way that only one of the two mirror-symmetric sites (above and below) is occupied, keeping the $P6_3/m$ symmetry. HApMnSi presents similar structural features.

while Sr(2) bonds to 6 oxygen atoms and one OH group. In HApMnSi, Mn and Si atoms occupy the same crystallographic site in a distorted tetrahedral coordination. The isotropic temperature factors were also refined. Table S1 shows the atomic parameters, the temperature factors, and the refined occupancies for Mn/Si and OH groups. According to NPD refinement, the final compositions are $Sr_5(MnO_4)_3(OH)$ and $Sr_5[(Mn_{0.947(6)}Si_{0.053(6)})O_4]_3(OH)_{0.82(2)}$ for HApMn and HApMnSi samples, respectively. These cationic compositions are in agreement with the electron microprobe results. The requirement for electroneutrality imposes a Mn oxidation state V [assuming Si(IV)] in both Si-free and Si-doped samples.

In HApMn and HApMnSi, two identical M−O3 distances (Table S2) (M = Mn/Si, ∼1.66 Å), one long M−O1 distance (∼1.71 Å), and a shorter one M−O2 at ∼1.65 Å are observed. The average M−O bond length (1.673 Å) is very similar to that found in other compounds constituted by isolated Mn(V) tetrahedra, such as in apatite-related $Ba_5(MnO_4)_3Cl$ (1.699(5) Å)[7] or in $Ba_3Mn_2O_8$ palmierite (1.697 Å).[5] Thus, the presence of Si in the tetrahedra (∼8.5% of these sites) does not modify the Mn−O average bond lengths.

In both hydroxyapatites, the hydroxyl groups are located in 4*e* sites displaced ∼0.4 Å from the mirror planes at $z = 1/4$ and $z = 3/4$ characteristic of the $P6_3/m$ symmetry. According to the general formula of the apatite, this site is half-occupied and the OH groups are statistically distributed in such a way that only one of the two mirror-symmetric sites (above and below) is occupied, keeping the $P6_3/m$ symmetry.

The detailed crystal structure was further assessed by TEM. The HApMn sample decomposed too quickly under the electron beam to enable structural analysis so that the study was focused on the HApMnSi sample, which was more stable, even if still sensitive, versus beam damage (Figures S4 and S5). Atomic-resolution scanning TEM (STEM) images and high-energy resolution EELS spectra were recorded on an aberration-corrected transmission electron microscope after optimization of the experimental conditions, in order to limit beam damage (see the Experimental Section and section V in Supporting Information-V).

Figure 4a shows an atomically resolved HAADF image of a representative HApMnSi crystal along the [001] direction in agreement with the apatite structure. The hexagonal arrangement of six Sr ($Z = 38$) atomic columns occupying Sr(1) sites is observed with the brightest contrast (marked with a yellow line). The image also allows identifying the hexagonal

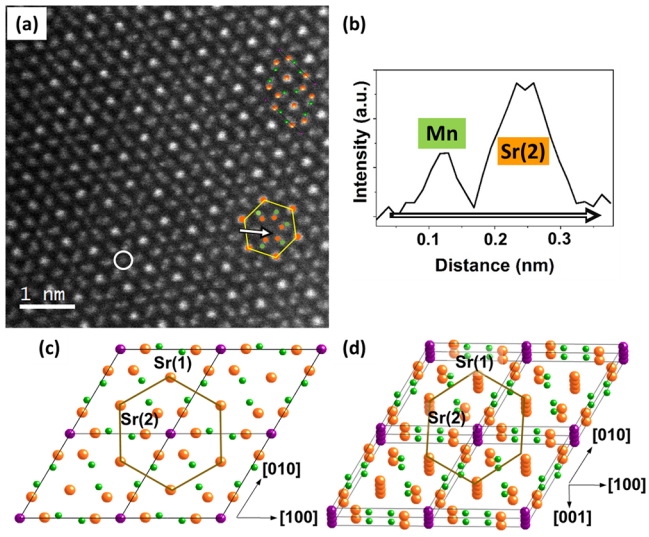

Figure 4. (a) HAADF image of a representative HApMnSi crystal along the [001] direction. A schematic representation of the apatite-type unit cell is shown as inset. The white circle highlights electron density in the center of the hexagonal cavities, corresponding to OH groups. (b) Intensity profile along the white arrow in (a) reveals the different intensities of Mn and Sr(2) atomic columns. (c) Schematic representation of 2 × 2 × 2 unit cells of HApMnSi along the [001] projection. (d) Visualization of the higher number of Sr atoms in the Sr(1) atomic columns with respect to the Sr(2) columns for a 2 × 2 × 2 unit cell of HApMnSi along the [001] direction. Color code: Sr orange, Mn green, OH purple, and O atoms are omitted for clarity.

arrangement of six darker atomic columns occupied by the lighter Mn atoms ($Z = 25$). Additionally, Figure 4a shows a set of atomic columns with bright intensity that corresponds to Sr atomic columns in the Sr(2) sites. The Sr(2) and Mn distribution is revealed by an intensity line profile (Figure 4b). Although both Sr(1) and Sr(2) sites are occupied by the same atoms, which would provide a similar contrast in the HAADF image, the higher number of Sr atoms in the Sr(1) atomic columns with respect to the Sr(2) columns along the [001] direction is responsible for the highest intensity of Sr(1) atomic columns (Figure 4c,d). Finally, despite the low scattering of oxygen and hydrogen atoms at high diffraction angles, simulation of HAADF images along the [001] zone axis qualitatively indicates that the observed contrast can be due to hydroxyl groups (Table S3, Figure S6, and the corresponding discussion in section IV in the Supporting Information).

Oxidation State of Manganese in Strontium/Manganese Hydroxyapatites. As a result of the compositional and structural characterization described above, the oxidation state of manganese in HApMnSi should be Mn(V). The Mn−$L_{2,3}$ EELS signal has been demonstrated to be highly sensitive to local variations of the Mn oxidation state.[32] In fact, Mn−$L_{2,3}$ EELS data have been extensively discussed in the literature from manganese-based compounds with Mn(II), Mn(III), and Mn(IV) oxidation states. However, no experimental data from the Mn(V)−$L_{2,3}$ edge have been reported as far as we know, either by X-ray absorption spectroscopy or by electron energy-loss near-edge spectroscopy (ELNES). This is probably due to the large tendency of Mn(V) to reduce at lower oxidation states under irradiation. In this work, we report for the first time the ELNES Mn−$L_{2,3}$ signal of an inorganic solid with Mn(V), which complements the previously reported Mn−$L_{2,3}$ ELNES collection for Mn(II), Mn(III), and Mn(IV). These

data provide valuable information for the elucidation of Mn oxidation states in inorganic solids. Figure 5 shows the ELNES

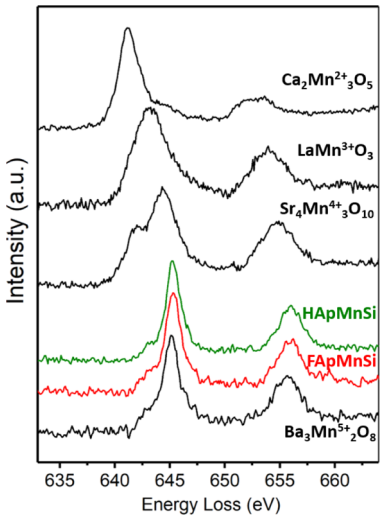

Figure 5. ELNES Mn−$L_{2,3}$ edges of references with Mn^{2+}, Mn^{3+}, Mn^{4+}, and Mn^{5+} oxidation states (black lines); HApMnSi (green) (spectrum acquired at room temperature), and FApMnSi (red) (spectrum acquired at low temperature). Mn is only at the Mn(V) state in both samples. The high degradation of the HApMn sample, as a result of its interaction with the electron beam even at low temperature, prevented the acquisition of a Mn−$L_{2,3}$ signal from the silicon-free sample (see the Supporting Information and Figure S8).

at the Mn−$L_{2,3}$ edge for manganese oxides with different oxidation states. The absolute energy of each Mn−$L_{2,3}$ edge was precisely calibrated with the zero-loss signal simultaneously acquired (see the Experimental Section), while the conditions have been optimized to avoid beam damage (see discussion in section V in Supporting Information V and Figure S7). A clear variation in the shape and the energy position is observed (Figure 5) as a function of the Mn oxidation state. Despite the different environments of manganese, being MnO_6 octahedral for the references with Mn^{2+}, Mn^{3+}, and Mn^{4+} and MnO_4 tetrahedral for HApMnSi, the Mn−$L_{2,3}$ edge corresponding to the HApMnSi material is visibly shifted to higher energy loss and reveals a shape different from the other signals. Because no Mn(V)−$L_{2,3}$ data have been reported in the literature, we have used $Ba_3Mn_2O_8$[5] with a palmierite-type structure as a reference, containing Mn(V) with $Mn^{V}O_4$ units similar to those observed in the present apatite samples. Under the same acquisition conditions, the EELS Mn−$L_{2,3}$ edges of HApMnSi and $Ba_3Mn_2O_8$ are identical (Figure 5), with very close $I(L_3)/I(L_2)$ ratios as well as energy loss positions of the L_3 and L_2 lines (Table S4). Therefore, we confirm the Mn(V) oxidation state of HApMnSi, and for the first time, we report an EELS Mn−$L_{2,3}$ signal corresponding to manganese with the high Mn(V) oxidation state.

Fluorine Doping of Strontium/Manganese Hydroxyapatites. Low-temperature fluorination routes have been widely used on mixed metal oxides to tune properties, such as magnetism or electrical and ionic conductivity, through topochemical modifications.[24] We have fluorinated the above-described hydroxyapatites at low temperature in order to preserve the apatite structure upon F-doping of HApMn (Figures 6a and 7a) and HApMnSi (Figures 6b and 7b). The XRD pattern of the fluorinated silicon-doped sample (labeled FApMnSi) did not show significant differences with respect to the starting HApMnSi sample, indicating that the apatite structure was maintained. The F content determined by electron microprobe analysis results in a Sr/Mn/Si/F molar cationic ratio close to 5:2.80:0.20:0.8. The structural parameters of the HApMnSi sample were used as a starting model for the refinement of NPD data. In a first refinement, all hydroxyl groups were replaced by fluoride ions. The scattering lengths of F and O atoms are too close (b_O = 5.803 fm; b_F = 5.654 fm) to distinguish them by NPD. Nonetheless, difference Fourier maps generated from NPD data did not show any negative scattering at $z \sim 0$ and $z \sim 0.5$ in the section $x = 0$ (Figure 6b), thus ruling out the presence of OH groups in the channels of the apatite structure. Hence, OH^- was fully substituted by F^- in FApMnSi, as supported by the satisfying resulting fit of NPD data (Figure 7b). The refined parameters, atom positions, and corresponding distances are listed in Tables S5 and S6. The crystallographic formula derived from NPD is $Sr_5[(Mn_{0.942(3)}Si_{0.058(3)})O_4]_3F_{0.83(1)}$, in agreement with electron microprobe analysis. No exchange of oxygen by fluorine in the $(Mn,Si)O_4$ units could be detected.

The NPD study of the Si-free fluoroapatite (FApMn) was performed using the abovedescribed OH-free Mn,Si-fluoroapatite as a starting structural model for refinement, leading to a satisfactory reliability (R_B = 2.04 and χ^2 = 4.75). The refined structure exhibits remaining hydrogen observed on the scattering density Fourier difference maps (Figure 6a) as weak negative scattering at $z \sim 0$ and ~0.5 in the section $x = 0$.

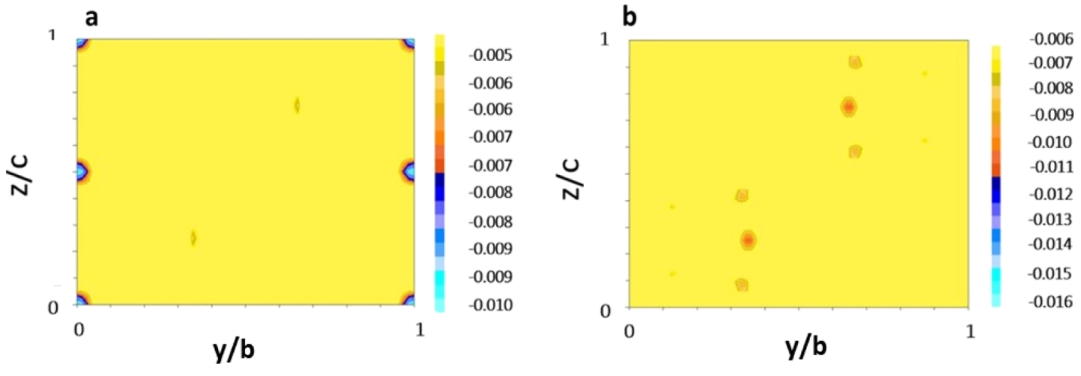

Figure 6. Difference Fourier maps of the section $x = 0$ for (a) FApMn and (b) FApMnSi. The maps show the positions in which the most prominent negative scattering density appears. The hydrogen atoms of the OH groups should be located at these positions in (a).

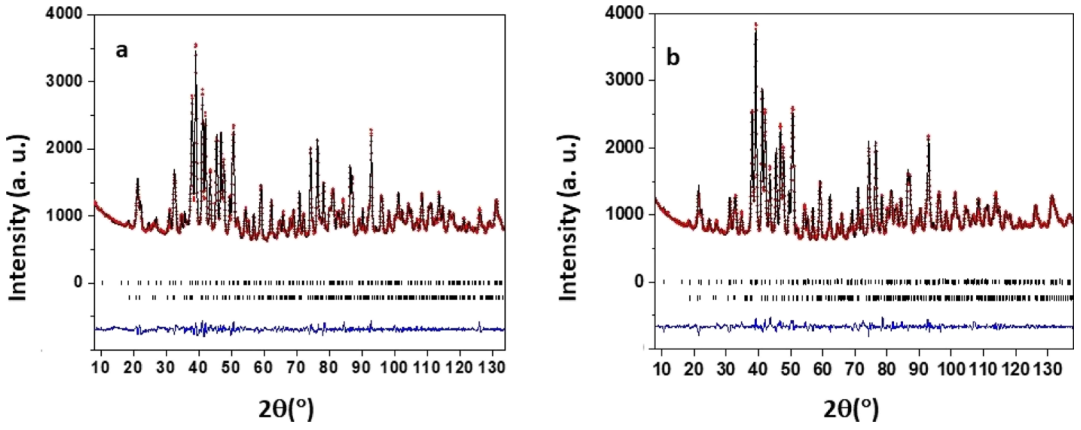

Figure 7. Final Rietveld refinement of the NPD data for (a) FApMn and (b) FApMnSi. The observed patterns (red circles), calculated patterns (continuous black line), and difference curves (continuous blue line) are shown. Upper tick marks correspond to the main apatite phase and lower ticks correspond to $SrCO_3$ added as a secondary phase.

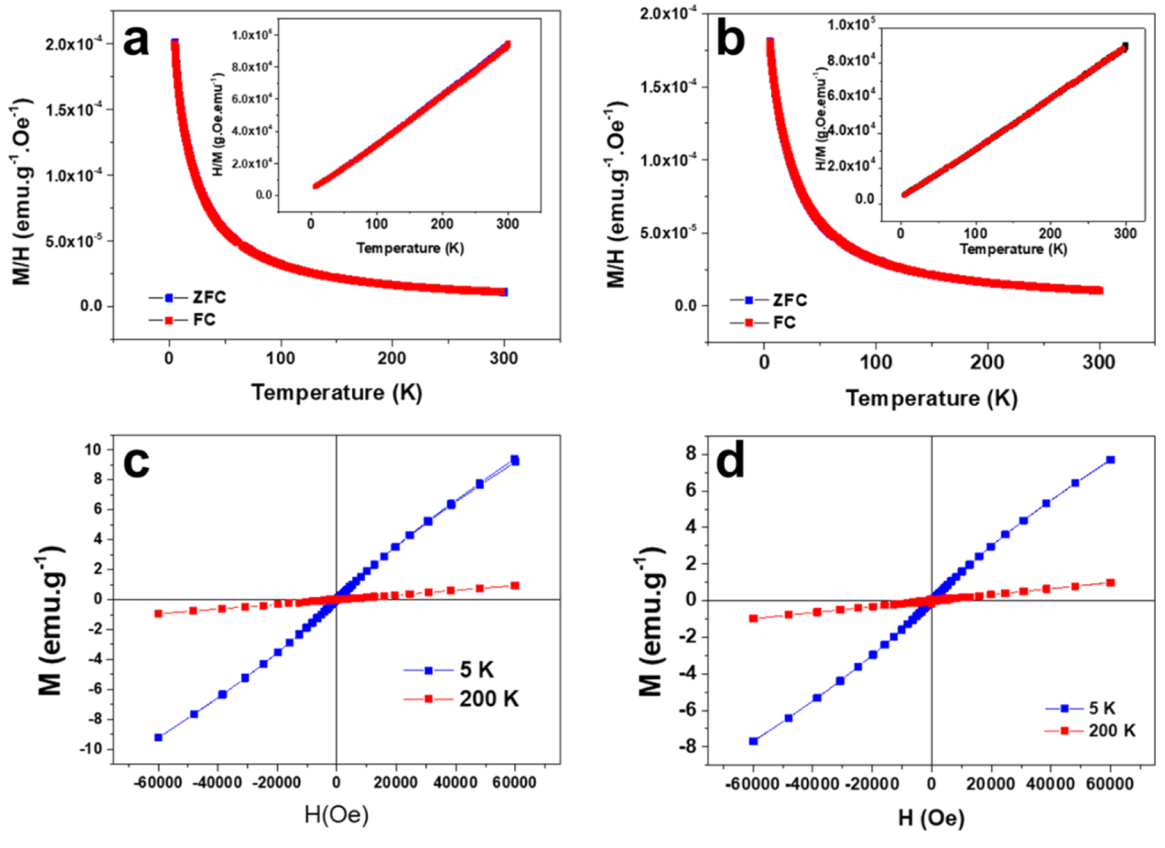

Figure 8. ZFC and FC magnetic susceptibility for (a) HApMnSi and (b) FApMnSi samples. Magnetization curves at 5 and 200 K for (c) HApMnSi and (d) FApMnSi samples.

Therefore, a new refinement (Figure 7a) was carried out by considering both F^- and OH^- anions in the channels of the apatite structure. From this, no more negative scattering was observed in the difference Fourier map. The derived crystallographic formula is $Sr_5(MnO_4)_3F_{0.90(2)}(OH)_{0.10(2)}$.

In the FApMn sample, although fluoride, the smallest anion, lies on the (a,b) planes at z = 1/4 and 3/4 (positions 0,0,1/4 and 0,0,3/4), the NPD refinement evidence that O_H atom is located off-plane with respect to the z F positions [at 0,0,0.19204(13)] as has already been observed in other hydroxyapatites.[31]

In both Si-free and Si-doped fluoroapatites, F^- incorporation occurs only in the channels by substitution of OH^- ions. The $Sr/(Mn,Si)O_4$ backbone is maintained. The decrease in the unit cell parameters from HApMn to FApMn and from HApMnSi to FApMnSi (see Table S7) is consistent with the substitution of OH^- ions by smaller F^- ions (ionic radii 1.34 and 1.30 Å, respectively).[14] As described in $Ca_5(PO_4)_3X$ (X: OH or F) apatites, F^- substitution mostly affects the a unit cell parameter, whereas c remains almost unchanged. This is related to the shortening of the Ca2−F bond length.[31]

Attempts to study the Mn oxidation state in the fluorinated samples by conventional EELS at room temperature were

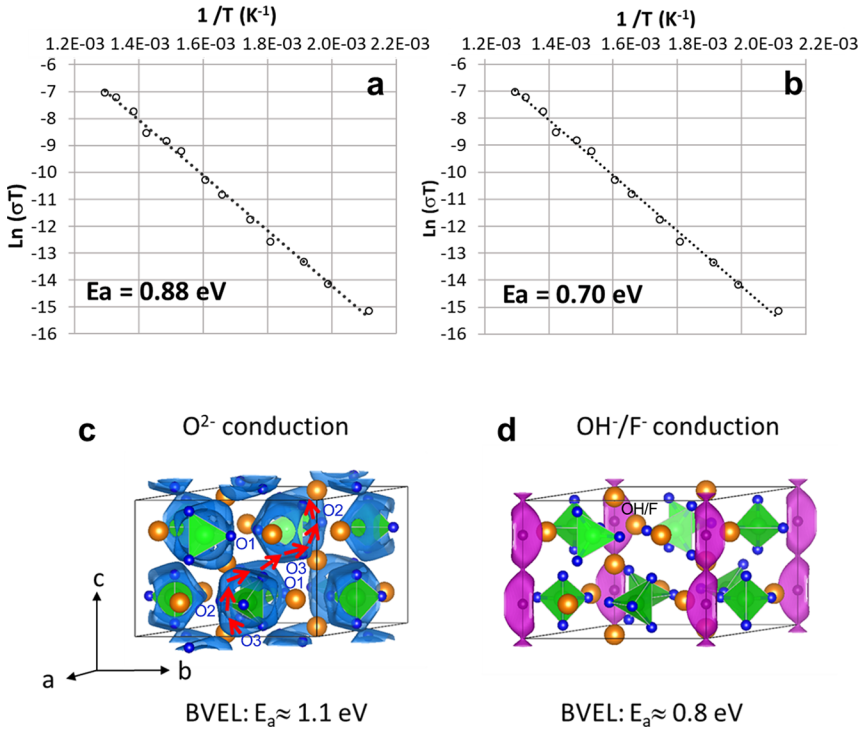

Figure 9. AC conductivity measurements as a function of temperature for (a) HApMnSi and (b) FApMnSi samples, with the corresponding linear fits. Anionic conduction paths deduced from BVEL calculations: (c) O^{2-} conduction paths are shown in blue with a percolation at 1.1 eV leading to a conduction along [001] (red arrows); (d) OH^-/F^- conduction paths (BVEL percolation at 0.8 eV) in the apatite channels running along [001] (purple). Color code: Sr, Mn, OH/F, and O atoms are orange, green, purple, and blue, respectively.

unsuccessful because of the poor stability of the F-doped samples under the electron beam. Then, EELS experiments were performed at low temperature (see section V in the Supporting Information). The Mn−$L_{2,3}$ edge (Figure 5) shows the features typical of Mn(V), confirming the isovalent substitution of F^- by OH^-, while keeping Mn in the sole (V) oxidation state.

Magnetic Properties of Strontium/Manganese Hydroxyapatites and Fluoroapatites. The magnetic behavior of all phases is similar. Figure 8 shows the magnetic susceptibility of HApMnSi and FApMnSi samples as a function of the temperature. A paramagnetic behavior is observed in the complete temperature range up to 300 K for both samples, as shown by the linear behavior of the inverse susceptibility versus T (Figure 8a,b). The paramagnetic moment calculated from the slope yields values of 3.0 and 2.63 μ_B/f.u. for HApMnSi and FApMnSi, respectively. The expected paramagnetic moment for the Mn^{5+} ion in the spin-only approximation is 2.83 μ_B. The agreement between the measured and expected values confirms the oxidation state (V) of Mn and the homogeneity of the oxidation state over the whole sample. In both samples, there is no indication of long-range order. However, weak and antiferromagnetic short-range interactions occur, as inferred from the measured Curie−Weiss temperatures Θ = −4.1 and −0.9 K for HApMnSi and FApMnSi, respectively. The field dependences of the magnetization at 200 K for HApMnSi and FApMnSi (Figure 8c,d) are linear, showing a pure paramagnetic system. However, at low temperature (5 K), a weak ferromagnetic-like behavior is observed with rather low coercive fields (47 and 63 Oe for HApMnSi and FApMnSi, respectively). At 5 K (Figure 8c,d), this weak ferromagnetic-like magnetization does not saturate. This contribution could arise from two origins. The first one is the presence of noncompensated spins at the surface of the grains. The other origin of the ferromagnetic-like component at low temperature is the balance of the short-range interactions within the next neighbor and the next-next neighbors, Mn^{5+} dimers (S = 1), already observed in, for example, $Ba_3Mn_2O_8$.[6,33] Depending on the energy balance between these interactions, a frustrated magnetic behavior arises that may result in a canted state, thus yielding the low-temperature ferromagnetic-like magnetization observed at 5 K for HApMnSi and FApMnSi (Figure 8c,d). A similar behavior is found in HApMn and FApMn (see Table S8 and Figures S9, S10).

Ionic Conductivity. The thermal stability of the samples was evaluated by TGA and *in situ* high-temperature XRD (HT-XRD). The HApMn sample starts to decompose at 500 °C (see section IX in the Supporting Information and Figures S11−S14) while incorporation of Si into HApMnSi stabilizes the solid up to 725 °C (Figure S11). The fluorinated phases exhibit a similar behavior: the FApMn decomposition starts around 450 °C while FApMnSi is stable up to 725 °C. The conductivity was then measured on pelletized samples from 200 to 500 °C for HApMnSi and FApMnSi (Figure 9a,b). As expected, the conductivity increases with the temperature, with activation energies of 0.88 and 0.70 eV for HApMnSi and FApMnSi, respectively. These values are similar or even lower than those reported for substituted oxyapatite-type lanthanum silicates.[34,35] Both samples exhibit conductivity values of the order 10^{-4} S cm^{-1} at 500 °C after correction of porosity effects (pellet porosity ∼40%).[36] These values are consistent with anionic conduction, especially O^{2-} conduction, and similar to those observed in oxyapatite-type lanthanum silicates.[34,35] Noteworthy, HApMnSi and FApMnSi achieve conductivity values similar to these silicates but 100 °C below, thus

evidencing significant ionic conduction properties. In order to get further insights into the ionic conductivity mechanism, we have calculated BVEL maps to identify the anionic conduction paths in HApMnSi and FApMnSi. Two different conductions paths were identified (Figure 9c,d). The first one (Figure 9c) corresponds to a pure O^{2-} conduction and goes through O1, O2, and O3 oxygen atoms surrounding Mn/Si. These conduction spheres percolate about 1.1 eV above the minimum energy to allow ionic conduction along the [001] direction (red arrows in Figure 9c). The second path (Figure 9d) revealed by BVEL calculations corresponds to the channels of the apatite structure. It is linear along *c* and involves either hydroxyl or F^- anions, with BVEL-calculated percolation energy of *ca.* 0.8 eV. Given the small difference in percolation energies and the measured activation energies, it is very likely that the two conduction mechanisms occur simultaneously in both HApMnSi and FApMnSi materials. They all relate to anionic conduction along the *c* axis, as observed in other apatite-like structure.[31]

CONCLUSIONS

In this work, we report four manganese (V) compounds with the hydroxyapatite structure, by revising the nominal $Sr_5(MnO_4)_3OH$ as a starting point to widen the range of apatite-related solids based on the $Mn^VO_4^{3-}$ framework. We took advantage of soft chemistry methods to tune the synthesis conditions in order to deliver silicon-doped $Sr_5[(Mn_{1-x}Si_x)O_4]_3(OH)_{1-3x}$ (x = 0.053). Additionally, post-treatment topochemical transformations allowed us to further extend the composition range toward fluoride-doped $Sr_5(MnO_4)_3(OH)_{1-y}F_y$ (y = 0.90) and $Sr_5[(Mn_{1-x}Si_xO_4)]_3F_{1-3x}$ (x = 0.058). Reproducible synthesis of these Sr-based apatite compounds opens new perspectives for unexplored compositions. The high Mn(V) oxidation state in these compounds, verified for the first time by local EELS spectroscopy and confirmed by the evaluation of the magnetic properties, yields the formation of $Mn^VO_4^{3-}$ building units, which constitute the scaffold of the apatite-type structure as fully described by the analysis of the NPD data. These rare-earth-free materials present significant anionic conduction and low corresponding activation energies at 500 °C. These values are reached at lower temperatures than for related apatite-type rare-earth element known as anionic conductors, thus initiating a novel approach in the design of materials for solid oxide fuel cells. Therefore, the combination of Mn(V) and significant anionic conduction supports the emergence of new solid functional materials which will be built from high-oxidation state manganese species.

SEM images of HApMn; structural analysis by X-ray and neutron diffraction of HApMn and HApMnSi samples; TEM experiments on the HApMnSi sample; HAADF image simulations of the HApMnSi material along the [001] projection; optimization of the STEM−EELS experimental conditions; EELS Mn−$L_{2,3}$ signal analysis; neutron diffraction data refinement of the fluorinated FApMn sample; magnetic behavior of HApMn and FApMn apatites; and thermal stability study of HApMnSi and HAPMn samples (PDF)

Crystallographic data of FApMn (CIF)

Crystallographic data of FApMnSi (CIF)

Crystallographic data of HApMn (CIF)

Crystallographic data of HApMnSi (CIF)

AUTHOR INFORMATION

David Portehault − *Sorbonne Université, CNRS, Collège de France, Laboratoire Chimie de la Matière Condensée de Paris, 75005 Paris, France;* orcid.org/0000-0003-4914-4913; Email: david.portehault@sorbonne-universite.fr

Marina Parras − *Departamento de Química Inorgánica, Facultad de Químicas, Universidad Complutense de Madrid, 28040 Madrid, Spain*; Email: mparras@ucm.es

Aurea Varela − *Departamento de Química Inorgánica, Facultad de Químicas, Universidad Complutense de Madrid, 28040 Madrid, Spain*

Isabel Gómez-Recio − *Departamento de Química Inorgánica, Facultad de Químicas, Universidad Complutense de Madrid, 28040 Madrid, Spain;* orcid.org/0000-0001-7788-9037

Laura Serrador − *Departamento de Química Inorgánica, Facultad de Químicas, Universidad Complutense de Madrid, 28040 Madrid, Spain*

María Hernando − *Departamento de Química Inorgánica, Facultad de Químicas, Universidad Complutense de Madrid, 28040 Madrid, Spain*

Emilio Matesanz − *Unidad de Difracción de Rayos X. Centro de Asistencia a la Investigación de Técnicas Físicas y Químicas, Universidad Complutense de Madrid, 28040 Madrid, Spain;* orcid.org/0000-0003-3147-8579

Almudena Torres-Pardo − *Departamento de Química Inorgánica, Facultad de Químicas and ICTS ELECMI Centro Nacional de Microscopía Electrónica, Universidad Complutense de Madrid, 28040 Madrid, Spain;* orcid.org/0000-0002-1667-4072

María Teresa Fernández-Díaz − *Institut Laue-Langevin, 38042 Grenoble cedex 9, France*

Jose L. Martínez − *Instituto de Ciencia de Materiales de Madrid, CSIC, 28049 Madrid, Spain*

Francisco Gonell − *Sorbonne Université, CNRS, Collège de France, Laboratoire Chimie de la Matière Condensée de Paris, 75005 Paris, France;* orcid.org/0000-0002-8658-2878

Gwenaelle Rousse − *Sorbonne Université, Collège de France, Chimie du Solide et de l'Energie, UMR 8260, Collège de France, 75007 Paris, France;* orcid.org/0000-0001-8877-0015

Clément Sanchez − *Sorbonne Université, CNRS, Collège de France, Laboratoire Chimie de la Matière Condensée de Paris, 75005 Paris, France;* orcid.org/0000-0002-6426-4844

Christel Laberty-Robert − *Sorbonne Université, CNRS, Collège de France, Laboratoire Chimie de la Matière Condensée de Paris, 75005 Paris, France;* orcid.org/0000-0003-3230-3164

José M. González-Calbet − *Departamento de Química*

Complutense de Madrid, 28040 Madrid, Spain;
orcid.org/0000-0002-6481-6506

Notes

The authors declare no competing financial interest.

ACKNOWLEDGMENTS

This work was supported by the Spanish Ministry of Innovation, Science and Technology and Spanish Ministry of Economy through Research Project MAT2017-82252-R and MAT2017-84496-R. We thank the National Facility ELECMI ICTS and CAI for XRD (UCM) for facilities. A.T.P. acknowledges financial support from the Comunidad de Madrid through the PR65/19 Research Project.

REFERENCES

(1) Hong, S.; Lee, Y.-M.; Sankaralingam, M.; Vardhaman, A. K.; Park, Y. J.; Cho, K.-B.; Ogura, T.; Sarangi, R.; Fukuzumi, S.; Nam, W. A Manganese(V)-Oxo Complex: Synthesis by Dioxygen Activation and Enhancement of Its Oxidizing Power by Binding Scandium Ion. *J. Am. Chem. Soc.* **2016**, *138*, 8523−8532.

(2) Mondal, S.; Naik, P. K.; Adha, J. K.; Kar, S. Synthesis, Characterization, and Reactivities of High Valent Metal−Corrole (M = Cr, Mn, and Fe) Complexes. *Coord. Chem. Rev.* **2019**, *400*, 213043.

(3) Ma, L.; Wang, Q.; Man, W.-L.; Kwong, H.-K.; Ko, C.-C.; Lau, T.-C. Cerium(IV)-Driven Water Oxidation Catalyzed by a Manganese(V)-Nitrido Complex. *Angew. Chem. Int. Ed.* **2015**, *54*, 5246−5249.

(4) Yano, J.; Robblee, J.; Pushkar, Y.; Marcus, M. A.; Bendix, J.; Workman, J. M.; Collins, T. J.; Solomon, E. I.; DeBeer George, S.; Yachandra, V. K. Polarized X-Ray Absorption Spectroscopy of Single-Crystal Mn(V) Complexes Relevant to the Oxygen-Evolving Complex of Photosystem II. *J. Am. Chem. Soc.* **2007**, *129*, 12989−13000.

(5) Weller, M. T.; Skinner, S. J. $Ba_3Mn_2O_8$ Determined from Neutron Powder Diffraction. *Acta Crystallogr. Sect. C Cryst. Struct. Commun.* **1999**, *55*, 154−156.

(6) Samulon, E. C.; Kohama, Y.; McDonald, R. D.; Shapiro, M. C.; Al-Hassanieh, K. A.; Batista, C. D.; Jaime, M.; Fisher, I. R. Asymmetric Quintuplet Condensation in the Frustrated S=1 Spin Dimer Compound $Ba_3Mn_2O_8$. *Phys. Rev. Lett.* **2009**, *103*, 047202.

(7) Medina, E. A.; Li, J.; Stalick, J. K.; Subramanian, M. A. Intense Turquoise Colors of Apatite-Type Compounds with Mn^{5+} in Tetrahedral Coordination. *Solid State Sci.* **2016**, *52*, 97−105.

(8) Knyazev, A. V.; Mączka, M.; Bulanov, E. N.; Ptak, M.; Belopolskaya, S. S. High-Temperature Thermal and X-Ray Diffraction Studies, and Room-Temperature Spectroscopic Investigation of Some Inorganic Pigments. *Dyes Pigm.* **2011**, *91*, 286−293.

(9) Scholder, R.; Klemm, W. Uber Neue Metallate Mit Sauerstoff Und Fluor als Liganden. *Angew. Chem.* **1954**, *66*, 461−467.

(10) Chance, W. M. *Hydroflux Synthesis: A New and Effective Technique for Exploratory Crystal Growth*; University South Carolina: USA, 2014; pp 1−268.

(11) Albrecht, R.; Doert, T.; Ruck, M. Hydroflux Synthesis and Characterization of the Non-Centrosymmetric Oxomanganate(V) $KSrMnO_4$. *Z. Anorg. Allg. Chem.* **2020**, *646*, 1389−1395.

(12) Dardenne, K.; Vivien, D.; Huguenin, D. Color of Mn(V) -Substituted Apatites $A_{10}((B,Mn)O_4)_6F_2$, A=Ba , Sr , Ca ; B=P , V. *J. Solid State Chem.* **1999**, *146*, 464−472.

(13) Baran, E. J.; Aymonino, P. J. Herstellung Und Eigenschaften Der Vervindungen $Sr_2(MnO_4)OH$ Und $Sr_2(MnO_4)OH.2H_2O$. *Monatsh. Chem.* **1969**, *100*, 1674−1683.

(14) White, T.; Ferraris, C.; Kim, J.; Madhavi, S. Apatite—an Adaptive Framework Structure. *Rev. Mineral. Geochem.* **2005**, *57*, 307−401.

(15) Kay, M. I.; Young, R. A.; Posner, A. S. Crystal Structure of Hydroxyapatite. *Nature* **1964**, *204*, 1050−1052.

(16) Elliot, J. C.; Wilson, R. M.; Dowker, E. E. P. Apatite Structures. *Adv. X Ray Anal.* **2002**, *45*, 172−181.

(17) Chernorukov, N. G.; Knyazev, A. V.; Bulanov, E. N. Phase Transitions and Thermal Expansion of Apatite-Structured Compounds. *Inorg. Mater.* **2011**, *47*, 172−177.

(18) Kasamatsu, S.; Sugino, O. First-Principles Investigation of Polarization and Ion Conduction Mechanisms in Hydroxyapatite. *Phys. Chem. Chem. Phys.* **2018**, *20*, 8744−8752.

(19) Tolchard, J. R.; Islam, M. S.; Slater, P. R. Defect Chemistry and Oxygen Ion Migration in the Apatite-Type Materials $La_{9.33}Si_6O_{26}$ and $La_8Sr_2Si_6O_{26}$. *J. Mater. Chem.* **2003**, *13*, 1956−1961.

(20) Sansom, J.; Richings, D.; Slater, P. R. Powder Neutron Diffraction Study of the Oxide-Ion-Conducting Apatite-Type Phases, $La_{9.33}Si_6O_{26}$ and $La_8Sr_2Si_6O_{26}$. *Solid State Ionics* **2001**, *139*, 205−210.

(21) León-Reina, L.; Losilla, E. R.; Martínez-Lara, M.; Martín-Sedeño, M. C.; Bruque, S.; Núñez, P.; Sheptyakov, D. V.; Aranda, M. A. G. High Oxide Ion Conductivity in Al-Doped Germanium Oxyapatite. *Chem. Mater.* **2005**, *17*, 596−600.

(22) Tate, M. L.; Blom, D. A.; Avdeev, M.; Brand, H. E. A.; McIntyre, G. J.; Vogt, T.; Evans, I. R. New Apatite-Type Oxide Ion Conductor, $Bi_2La_8[(GeO_4)_6]O_3$: Structure, Properties, and Direct Imaging of Low-Level Interstitial Oxygen Atoms Using Aberration-Corrected Scanning Transmission Electron Microscopy. *Adv. Funct. Mater.* **2017**, *27*, 1605625 DOI: 10.1002/adfm.201605625.

(23) Ptáček, P. *Apatites and Their Symthetic Analogues. Synthesis, Structure, Properties and Applications*; IntechOpen, 2016; pp 45−288.

(24) Clemens, O.; Slater, P. R. Topochemical Modifications of Mixed Metal Oxide Compounds by Low-Temperature Fluorination Routes. *Rev. Inorg. Chem.* **2013**, *33*, 105−117.

(25) González Hernando, M.; Fernández-Díaz, M. T.; Gómez-Recio, I.; Matesanz, E.; Marina, P.; Varela, A. *Stabilisation of Sr-Manganese Phases with an Unusual Manganese Oxidation State*; Institute Laue-Langevin (ILL), 2016 DOI: 10.5291/ILL-DATA.5-21-1104.

(26) Rietveld, H. M. A Profile Refinement Method for Nuclear and Magnetic Structures. *J. Appl. Crystallogr.* **1969**, *2*, 65−71.

(27) Rodríguez-Carvajal, J. Recent Advances in Magnetic Structure Determination by Neutron Powder Diffraction. *Phys. B* **1993**, *192*, 55−69.

(28) Adams, S. From Bond Valence Maps to Energy Landscapes for Mobile Ions in Ion-Conducting Solids. *Solid State Ionics* **2006**, *177*, 1625−1630.

(29) Katcho, N. A.; Carrete, J.; Reynaud, M.; Rousse, G.; Casas-Cabanas, M.; Mingo, N.; Rodríguez-Carvajal, J.; Carrasco, J. An Investigation of the Structural Properties of Li and Na Fast Ion Conductors Using High-Throughput Bond-Valence Calculations and Machine Learning. *J. Appl. Crystallogr.* **2019**, *52*, 148−157.

(30) Zagorac, D.; Müller, H.; Ruehl, S.; Zagorac, J.; Rehme, S. Recent Developments in the Inorganic Crystal Structure Database: Theoretical Crystal Structure Data and Related Features. *J. Appl. Crystallogr.* **2019**, *52*, 918−925.

(31) Hughes, J. M.; Cameron, M.; Crowley, K. D. Structural Variations in Natural F, OH, and Cl Apatites. *Am. Mineral.* **1989**, *74*, 870−876.

(32) González-Jiménez, I. N.; Torres-Pardo, A.; Sánchez-Peláez, A. E.; Gutiérrez, A.; García-Hernández, M.; González-Calbet, J. M.; Parras, M.; Varela, Á. Synthesis of 4H-$SrMnO_{3.0}$ Nanoparticles from a Molecular Precursor and Their Topotactic Reduction Pathway Identified at Atomic Scale. *Chem. Mater.* **2014**, *26*, 2256−2265.

(33) Samulon, E. C.; Jo, Y.-J.; Sengupta, P.; Batista, C. D.; Jaime, M.; Balicas, L.; Fisher, I. R. Ordered Magnetic Phases of the Frustrated Spin-Dimer Compound $Ba_3Mn_2O_8$. *Phys. Rev. B: Condens. Matter Mater. Phys.* **2008**, *77*, 1−13.

(34) Funahashi, T.; Mineshige, A.; Yoshioka, H.; Kobayashi, K.; Matsushita, Y.; Katsuya, Y.; Tanaka, M.; Sakata, O.; Yazawa, T. Effect of Cation Doping on Ionic Conductivity and Crystal Structure of Oxyapatite-Type Lanthanum Silicates. *Solid State Ionics* **2016**, *289*, 106−112.

(35) Abram, E. J.; Sinclair, D. C.; West, A. R. A Novel Enhancement of Ionic Conductivity in the Cation-Deficient Apatite $La_{9.33}(SiO_4)_6O_2$. *J. Mater. Chem.* **2001**, *11*, 1978−1979.
(36) Muller, G.; Ringuedé, A.; Laberty-Robert, C. Discussion on a Percolating Conducting Network of a Composite Thin-Film Electrode ($\leq$1 μm) for Micro-Solid Oxide Fuel Cell Application. *Langmuir* **2014**, *30*, 8889−8897.